Numerical analysis of disbonding in sandwich structures using 1D finite elements

(Article begins on next page)

17 April 2024

Numerical analysis of disbonding in sandwich structures using 1D finite elements

L. Qi[1,2], M.H. Nagaraj[2], E. Carrera[2], C.F. Gao[1], M. Petrolo[2]

[1]State Key Laboratory of Mechanics and Control of Mechanical Structures, Nanjing University of Aeronautics and Astronautics, Nanjing 210016, China
[2]MUL2 Group, Department of Mechanical and Aerospace Engineering, Politecnico di Torino, Corso Duca degli Abruzzi 24, 10129 Torino, Italy

Author for correspondence:
Marco Petrolo
MUL[2] Group, Department of Mechanical and Aerospace Engineering,
Politecnico di Torino,
Corso Duca degli Abruzzi 24,
10129 Torino, Italy,
tel: +39 011 090 6845,
fax: +39 011 090 6899,
e-mail: marco.petrolo@polito.it

1

Abstract

Structural theories based on 1D component-wise models are proposed to investigate the progressive disbonding in sandwich structures. The structural framework adopts the Carrera Unified Formulation to generate higher-order theories of structures via a variable kinematic approach. The component-wise approach, formulated within the Lagrange polynomial based CUF models, permits modelling of various components of a complex structure through 1D CUF models at reduced computational costs and 3D accuracy. The disbonding constitutive models are retrieved from well-established works in the literature and based on cohesive elements. The results verify the accuracy of 1D models with some 10-20% computational time as compared to 3D finite elements.

Keywords: disbonding, sandwich structures, CUF, FEM, cohesive elements.

1 Introduction

Due to the superior stiffness-weight ratio as compared to traditional materials, composite sandwich structures are of high interest for aerospace and naval structures. Delamination and disbonding are common failure modes for this kind of structures. Typical triggers are the mismatch of material properties and defects introduced during the manufacturing process. The delamination and disbonding can result in a significant reduction in the load-bearing capacity of the structure, and the analysis of the initiation and propagation of failure is essential.

Early research on delamination and disbonding problems of composite sandwich structures relied on experimental methods [1, 2, 3, 4]. Subsequently, the research activity considered the use of the finite element method (FEM) to support experimental results [5, 6, 7]. In FEM, the cohesive method proposed by Dugdale [8] and Barenblatt [9] is a common tool for modelling the delamination or fracture, and has applications in various fields, such as biomechanics [10], electro-mechanical coupling [11, 12], and mixed-mode layering in composite materials [13, 14, 15]. Examples of works with cohesive elements and sandwich structures are those by Hower et al. [16, 17] with investigations on the pure mode-I disbonding of face/core interface via bilinear cohesive elements. The use of numerical frameworks for this class of problems involves nonlinear solvers and the use of 3D elements to detect transverse stresses. Such features make the computational costs high and preclude the analysis of complex structures and the use in non-academic environments. The use of shell elements can alleviate the computational overhead compared to 3D solid elements, and, recently, some works have focused on delamination problems [18, 19]. However, the use of such models may not be sufficiently accurate as sandwich structures with soft cores are analyzed, as higher-order layer-wise models can be necessary [20].

The prime purpose of this work is to verify the accuracy and computational efficiency

of 1D structural models for progressive disbonding in sandwich structures via cohesive elements. The structural theories are higher-order and generated by the Carrera Unified formulation (CUF), a framework for generating various classes of structural theories by varying the kinematic definitions [21]. The 1D component-wise (CW) [22] approach employed in this work can efficiently model the cohesive kinematics and simulate the interface behavior. Previous works include the introduction of cohesive elements in the CUF framework and its use in delamination modelling [23], and the present work focuses on the extension of the framework to disbonding of sandwich structures. Moreover, CUF models can handle the severe transverse anisotropy of sandwich structures with soft cores [24]. The present work is organized in the following manner: Section 2 introduces higher-order structural theories based on 1D-CUF, as well as the theory and constitutive laws for the cohesive model. The finite element formulation, for both the bulk and cohesive elements, is presented in Section 3. A series of numerical assessments are performed to demonstrate the capability of the proposed framework in the analysis of disbonding in sandwich structures, and is given in Section 4. Finally, the main conclusions of the present work are highlighted in Section 5.

2   1D CUF and cohesive models

Assuming an orthogonal reference frame in which the beam axis is parallel to the y-axis, the displacement field in CUF is

$$\mathbf{u} = F_\tau \left(x, z \right) \mathbf{u}_\tau \left(y \right), \ \ \tau = 1, ..., M \tag{1}$$

$$\mathbf{u} = \left\{ \begin{matrix} u_x & u_y & u_z \end{matrix} \right\}^{\mathrm{T}} \tag{2}$$

$F_\tau \left(x, z \right)$ are cross-sectional expansion functions [21] allowing for the use of any structural theory. M is the number of terms in the expansion function. $\mathbf{u}_\tau$ are generalized displace-

ments defined over the beam axis. There are various implementable classes of expansion functions, such as Taylor, Lagrange and Legendre polynomials, or trigonometric and exponential functions. Still, there is no need for formal modifications of the equations as the expansion and its order do not affect the governing equations of CUF. The current work uses Lagrange Expansions (LE), which are based on Lagrange polynomials and are implemented in the form of 9-node second-order quadrilateral element (L9), providing a higher-order model based on pure displacements. LE leads to 1D component-wise models (CW) [24], allowing to retain material and geometrical characteristics of each component of a structure. A six-node cohesive Lagrange cross-section element, as shown in Fig. 1, is introduced with expansion functions expressed as

$$\mathbf{u}^+ = F_1\mathbf{u}_4 + F_2\mathbf{u}_5 + F_3\mathbf{u}_6$$
$$\mathbf{u}^- = F_1\mathbf{u}_1 + F_2\mathbf{u}_2 + F_3\mathbf{u}_3 \tag{3}$$

$$F_1 = \tfrac{1}{2}\xi\left(1-\xi\right)$$
$$F_2 = -\left(1-\xi\right)\left(1+\xi\right)$$
$$F_3 = \tfrac{1}{2}\xi\left(1+\xi\right) \tag{4}$$

$$\xi_1 = -1,\ \xi_2 = 0,\ \xi_3 = 1 \tag{5}$$

where $\mathbf{u}^+$ and $\mathbf{u}^-$ are the displacements of the upper and lower surfaces of the interface, respectively. A mixed-mode cohesive constitutive model proposed by Camanho et al. [15] is adopted in this work. Based on the damage mechanics theory, the cohesive constitutive law relates the cohesive traction t_j to the displacement jump Δ_j in the local coordinate system [25],

$$t_j = (1-d)\,D_{ij}^0\Delta_j - dD_{ij}^0\delta_{3j}\left\langle-\Delta_3\right\rangle \tag{6}$$
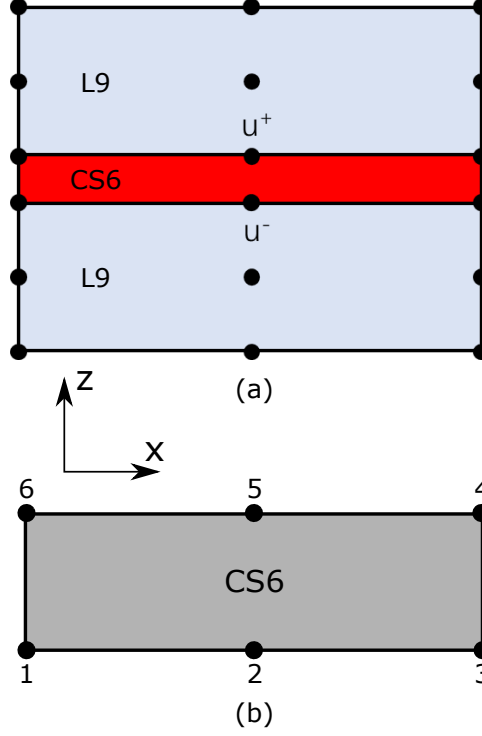
Figure 1: (a) Six-node cohesive Lagrange cross-section element (CS6) inserted between two bulk L9 elements, and (b) Topology of a CS6 cohesive element with node numbering.

in which the second term prevents non-physical post-decohesion interfacial penetrations. d is the damage variable, $<>$ is the MacAuley bracket and D_{ij}^0 is the initial stiffness tensor, which is defined as a function of the penalty parameter K and Kronecker delta δ_{ij},

$$D_{ij}^0 = \delta_{ij} K \tag{7}$$

The damage variable d makes use of a damage criterion built within the equivalent displacement jump space,

$$F\left(\lambda^t, r^t\right) = G\left(\lambda^t\right) - G\left(r^t\right) \leqslant 0 \; \forall \; t \geqslant 0 \tag{8}$$

6

where t denotes the quasi-static time and r^t is the damage threshold for the current time. Based on the mixed-mode bilinear constitutive formulation,

$$G(\lambda) = \frac{\Delta^f (\lambda - \Delta^0)}{\lambda (\Delta^f - \Delta^0)} \tag{9}$$

$$d^t = G(r^t) \ \forall \ r^t = \max_s \{r^0, \lambda\} \ 0 \geqslant s \geqslant t \tag{10}$$

where Δ^0 and Δ^f are the equivalent displacements at the beginning of damage and complete failure $(d = 1)$, respectively. λ is the current equivalent non-negative displacement jump.

The propagation criteria depends on the formulation presented by Benzeggagh and Kenane [26], which is a function of mode I and mode II fracture toughness, mode mixity and an experimentally obtained parameter η.

$$G_c = G_I^c + (G_{II}^c - G_I^c) \left(\frac{G_I^c}{G_T}\right)^\eta, \ G_T = \frac{G_{II}}{G_I + G_{II}} \tag{11}$$

The displacement jump criterion is

$$\Delta^0 = \sqrt{\Delta_3^2 + (\Delta_{\text{shear}}^2 - \Delta_3^2) B^\eta} \tag{12}$$

$$B = \frac{G_{\text{shear}}}{G_T}, \Delta_{\text{shear}} = \sqrt{\Delta_I^2 + \Delta_{II}^2}, G_{\text{shear}} = G_I + G_{II} \tag{13}$$

By differentiating the traction-displacement relationship in Eq. 6, the tangent constitutive matrix is derived [25] as follows

$$\dot{t} = D_{ij}^{\text{tan}} \dot{\Delta}_j \tag{14}$$

$$D_{ij}^{\text{tan}} = \begin{cases} \left\{D_{ij} - K \left[1 + \delta_{3j} \frac{\langle -\Delta_j \rangle}{\Delta_j}\right] \left[1 + \delta_{3j} \frac{\langle -\Delta_i \rangle}{\Delta_i}\right] H \Delta_i \Delta_j, r < \lambda < \Delta^f\right\} \\ D_{ij}, r > \lambda \ \text{or} \Delta^f < \lambda \end{cases} \tag{15}$$

where H is the scalar parameter defined as

$$H = \frac{\Delta^f \Delta^0}{\left(\Delta^f - \Delta^0\right) \lambda^3} \tag{16}$$

3   Finite element formulation

Under the assumption of small deformation, the linear stress-strain law is as follows

$$\boldsymbol{\sigma} = \mathbf{C}\boldsymbol{\varepsilon} \tag{17}$$

$$\boldsymbol{\varepsilon} = \mathbf{D}\mathbf{u} \tag{18}$$

where $\boldsymbol{\sigma} = \{\sigma_{xx}, \sigma_{yy}, \sigma_{zz}, \sigma_{yz}, \sigma_{xz}, \sigma_{xy}\}^{\mathrm{T}}$ and $\boldsymbol{\varepsilon} = \{\varepsilon_{xx}, \varepsilon_{yy}, \varepsilon_{zz}, \varepsilon_{yz}, \varepsilon_{xz}, \varepsilon_{xy}\}^{\mathrm{T}}$. $\mathbf{C}$ is the matrix of the material elastic properties and $\mathbf{D}$ is the differential operator defined as follows:

$$\mathbf{D}^{\mathrm{T}} = \begin{bmatrix} \partial_x & 0 & 0 & 0 & \partial_z & \partial_y \\ 0 & \partial_y & 0 & \partial_z & 0 & \partial_x \\ 0 & 0 & \partial_z & \partial_y & \partial_x & 0 \end{bmatrix} \tag{19}$$

By introducing the standard FE shape functions, the generalized displacement field becomes

$$\mathbf{u} = N_i\left(y\right) F_\tau\left(x, z\right) \mathbf{u}_{\tau i}\left(y\right) \quad \forall \ \ \tau = 1, 2, ..., M \ \ i = 1, 2, ..., p+1 \tag{20}$$

$$\mathbf{u}_{\tau i} = \begin{bmatrix} u_{x_{\tau i}} & u_{y_{\tau i}} & u_{z_{\tau i}} \end{bmatrix} \tag{21}$$

where N_i is the beam shape function of order p. $\mathbf{u}_{\tau i}$ is the nodal displacement vector. The choice of the shape function order p and the expansion function terms M remain independent and are input of the analysis. Then, the displacement fields on the upper

and lower interface of the cohesive elements (CS6) can be expressed as

$$\mathbf{u}^+ = F_\tau N_i \mathbf{u}_{\tau i}^+, \mathbf{u}^- = F_\tau N_i \mathbf{u}_{\tau i}^- \tag{22}$$

The displacement jump across the cohesive element surface will be

$$[[\mathbf{u}]] = F_\tau N_i \left(\mathbf{u}_{\tau i}^+ - \mathbf{u}_{\tau i}^- \right) \tag{23}$$

The displacement jump is computed as the difference between the displacements at the upper and lower edge of the CS6 cohesive element, whose values are calculated using the nodal displacements in combination with the shape and expansion functions. The tractions are computed at the integration points of the CS6 element. The equilibrium equations in terms of FE matrices become [21]

$$\mathbf{k}_{ij\tau s}^{\text{bulk}} \mathbf{u}_{\tau i} + \mathbf{k}_{ij\tau s}^{\text{coh}} [[\mathbf{u}_{\tau i}]] - \mathbf{p}_{\tau i} = 0 \tag{24}$$

where the $\mathbf{k}_{ij\tau s}^{\text{bulk}}$ and $\mathbf{k}_{ij\tau s}^{\text{coh}}$ present the Fundamental Nuclei (FNs) of the bulk and cohesive stiffness matrix, respectively. The $\mathbf{p}_{\tau i}$ is the external loading of FN. The FN of cohesive forces is [23]

$$f_{\text{coh}\tau i}^+ = \int_{\Gamma_c} F_\tau N_i \mathbf{u}_{\tau i}^+ t^+ d\Gamma_c, f_{\text{coh}\tau i}^- = \int_{\Gamma_c} F_\tau N_i \mathbf{u}_{\tau i}^- t^- d\Gamma_c \tag{25}$$

The rate form of the cohesive constitutive law is Eq. 14 [25],

$$\dot{\mathbf{t}}^c = \mathbf{Q}\mathbf{D}^{\text{tan}}\mathbf{Q}^{\text{T}} [[\dot{\mathbf{u}}]] = \mathbf{Q}\mathbf{D}^{\text{tan}}\mathbf{Q}^{\text{T}} F_\tau N_i \left(\mathbf{u}_{\tau i}^+ - \mathbf{u}_{\tau i}^- \right) \tag{26}$$

where $\mathbf{Q}$ is the orthogonal transformation matrix of the system for transforming local and global cohesive elements. The FN of the cohesive tangent matrix stems from the

linearization of the cohesive force vector (Eq. 25),

$$k_{ij\tau s}^{\text{coh}} = \int_{\Gamma_{\text{c}}} F_\tau N_i \mathbf{Q} \mathbf{D}^{\text{tan}} \mathbf{Q}^{\text{T}} F_s N_j d\Gamma_{\text{c}} \tag{27}$$

The integration of cohesive elements via the standard Gauss quadrature results in responses with spurious oscillations, especially when there are large stress gradients across a cohesive element. Consequently, The Newton-Cotes integration scheme is employed in this work to integrate the FN tangent stiffness matrix and internal force vector. The weak form of discrete equation is as follows

$$\mathbf{f}^{\text{int}} + \mathbf{f}^{\text{coh}} - \mathbf{f}^{\text{ext}} = 0 \tag{28}$$

where $\mathbf{f}^{\text{int}}$, $\mathbf{f}^{\text{coh}}$ and $\mathbf{f}^{\text{ext}}$ denote the global vectors for internal, cohesive and external forces, respectively. Based on the energy release rate, an arc-length solver with a path-following constraint [27, 28] is implemented in this work. Then, the global system of equation becomes

$$\begin{bmatrix} \mathbf{f}^{\text{int}}(\mathbf{u}) - \lambda\mathbf{f}^{\text{ext}} \\ g(\mathbf{u}, \lambda) \end{bmatrix} = 0 \tag{29}$$

$$g = \frac{1}{2}\mathbf{f}_{\text{ext}}^{\text{T}}(\lambda_0\Delta\mathbf{u} - \Delta\lambda\mathbf{u}_0) - \Delta\tau \tag{30}$$

where $\mathbf{f}^{\text{int}}(\mathbf{u})$ includes contributions from bulk as well cohesive finite elements and g is the energy-release constraint equation. $\mathbf{f}_{\text{ext}}^{\text{T}}$ denotes the global unit external force vector. $\Delta\tau$ is the dissipation path parameter, λ_0 and $\mathbf{u}_0$ are the last converged load factor and displacement vector, respectively. Given the best iteration value of each increment k_{opt}, the path parameter of the given increment i is [27]

$$\Delta\tau^i = \Delta\tau^{i-1}\frac{k_{\text{opt}}}{k^{i-1}} \tag{31}$$

10

where k_{opt} and k^{i-1} is the number of iterations required in the last converged loading step.

4 Numerical results

4.1 Single cantilever beam

This section presents the numerical results concerning a single cantilever beam (SCB), see Fig. 2. The load is introduced through a block bonded to the end of top facesheet above the pre-crack. The bottom facesheet is clamped. The parameters of the materials and cohesive layer can be found in Table 1. The numerical results from 1D CUF are
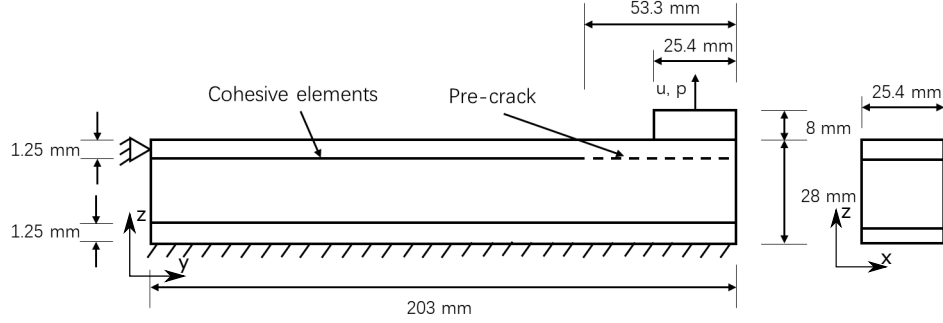

Figure 2: A schematic representation of the single cantilever beam (SCB). The sandwich structure is composed of a soft core with top and bottom facesheets made with an isotropic material.

Table 1: Material properties of the constituents of the SCB [16]

Facesheet				Load block	
E [MPa]	ν			E [MPa]	ν
86,593.9	0.311			72,000	0.3
Core					
$E_{\parallel}$ [MPa]	$E_{\perp}$ [MPa]	$\nu_{\perp\parallel}$	$\nu_{\perp}$	$G_{\perp}$ [MPa]	$G_{\perp\parallel}$ [MPa]
517.1*	0.1467	0.33	0.0001	0.03669	151.68*
Cohesive layer					
T^{max} [MPa]	G_{Ic} [J/m^2]	K_0 [MPa]			
0.5	1,050	75			

11

verified via 3D FE solutions and validated with experimental results from the literature [16]. In CUF, the mesh configuration of the cross-section is 2×6 L9 elements for the composite part, 2×2 L9 for the loading block, and 2 CS6 cohesive elements. Furthermore, more refined discretizations were used to test convergence, see Table 2. The refinement of the discretization was carried out along x. Along the length, 80 B4 cubic elements were used. The thickness of the cohesive layer in the CUF models is of the order 10^{-7} m; it does not significantly affect the global stiffness of the structure. In the ABAQUS analysis, the full integration standard continuum quadratic elements were used for the facesheets, core, and load introduction block. A schematic representation of the cross-section mesh used in both models is shown in Fig. 3. The discretisation used in both approaches were determined on the basis of a mesh convergence study, whose results are plotted in Fig. 4. The comparison of the details between these two methods and an FE model from the literature is shown in Table 2. The time reported in the present work refers to real (wall) time. All the analyses in the present work consider geometrical linearity, with nonlinearity arising from the cohesive constitutive law. The ABAQUS models are solved using the Riks method, while CUF utilises an arc-length approach with an energy-dissipation constraint as described at the end of Section 3.

The SCB load-displacement curves are shown in Fig. 5, along with reference numerical and experimental data from the literature [16]. In Table 3, some of the load-displacement values are reported. The comparison of deformation patterns in CUF and ABAQUS is given in Fig. 6 when displacement of the load point, u, is 26mm and 36mm, respectively.

The numerical results show that

- The pre-peak portion of the equilibrium curves are identical for CUF and the 3D FE model. Some differences are visible, considering the FE results from the literature and the experiment. The differences between the two sets of numerical models may be due to the use of plane stress elements in [16].
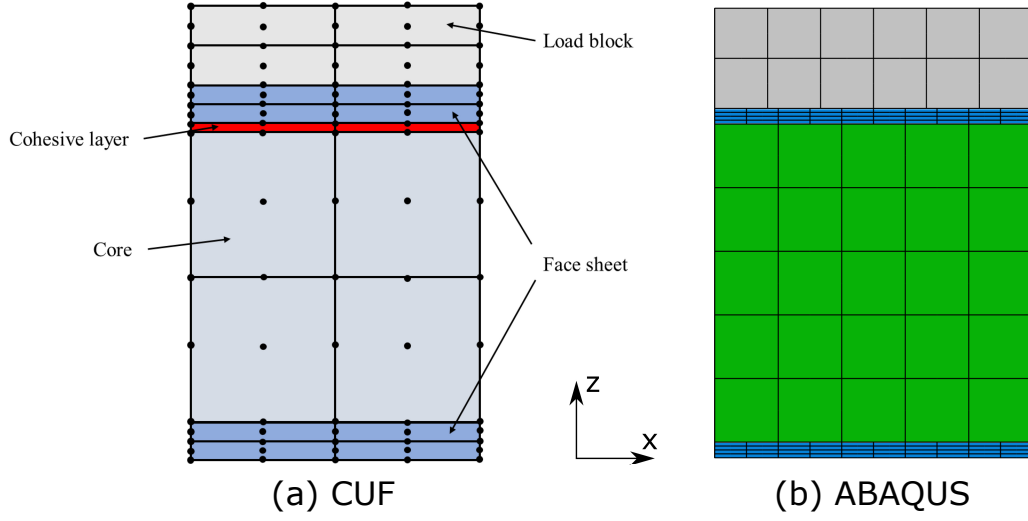
Figure 3: Schematic representation of the cross-section mesh used in the CUF (2×6 L9) and ABAQUS (Mesh-2) models

Table 2: Model information on the various numerical approaches used for the SCB

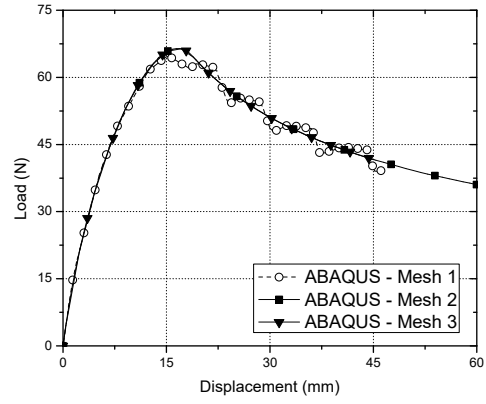| Methods	Discretisation	Total nodes	DOF	Time* (hh:mm:ss)
CUF - 2×6L9	12L9-2CS6-80B4	17,190	51,570	00:17:35
CUF - 4×6L9	24L9-4CS6-80B4	30,456	91,368	01:03:00
CUF - 6×6L9	36L9-6CS6-80B4	43,992	131,976	01:52:20
ABAQUS - Mesh 1	C3D20-COH3D8	36,300	108,942	01:32:07
ABAQUS - Mesh 2	C3D20-COH3D8	67,372	202,158	03:26:47
ABAQUS - Mesh 3	C3D20-COH3D8	90,189	270,609	04:55:29
Höwer [16]	CPS4R-user elements	191,621	N/A	N/A

* The reported run-times are based on analyses performed on a laptop using a single core.

Table 3: Load-displacement values for the SCB

Displacements [mm]	Loads [N]		Difference [%]
	CUF	ABAQUS	
Peak Load	67.768	66.596	1.76
5	34.977	35.973	0.64
10	56.112	55.666	0.80
20	65.026	62.733	3.65
30	52.997	51.104	3.70
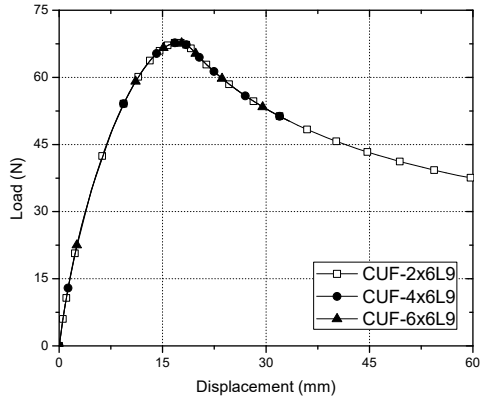
(a) CUF convergence study   (b) ABAQUS convergence study

Figure 4: Load-displacement response obtained from a mesh convergence study for the CUF and ABAQUS models
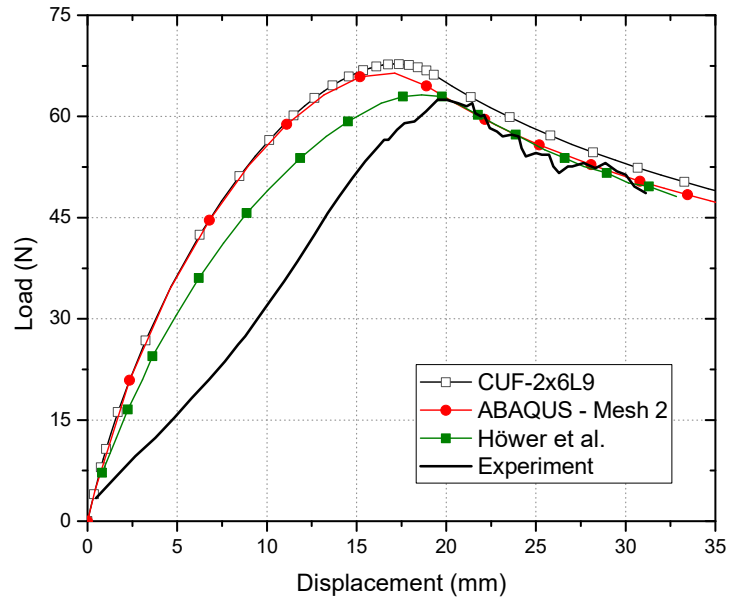

Figure 5: Load-displacement curves obtained from the CUF and ABAQUS solutions of the SCB test. Reference numerical and experimental data is obtained from [16].

(a) CUF, U=26 mm   (b) CUF, U=36 mm

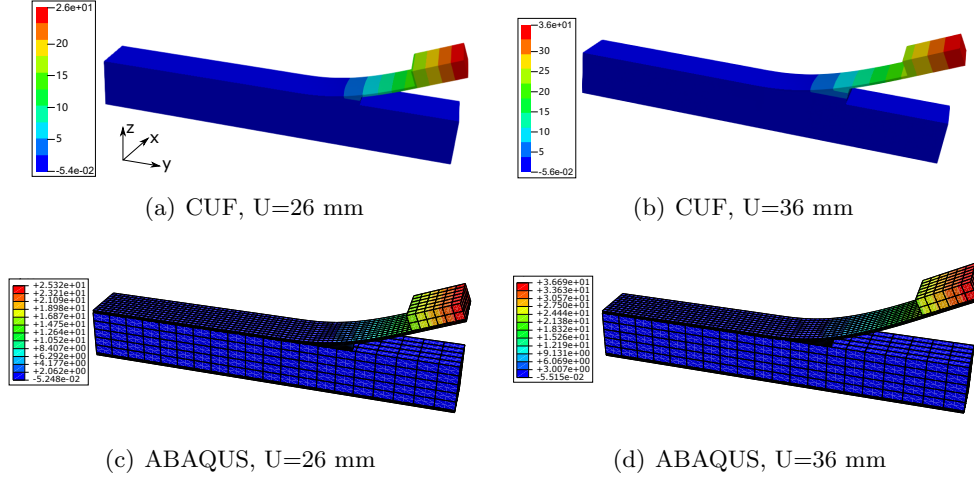(c) ABAQUS, U=26 mm   (d) ABAQUS, U=36 mm

Figure 6: 3D displacement profile of the SCB at various load levels

- The post-peak curves are all quite close with differences ranging from 1.7 to 3.7%. For a given load value, the CUF result has higher displacements.

- The computational time of the CUF models is some 10% the one of 3D FE.

4.2 Double cantilever beam

In this section, the same cohesive parameters and geometry dimensions of SCB - Table 1 - but without the load block, were employed to simulate the double cantilever beam model (DCB), see Fig. 7. The differences from SCB are the boundary conditions and loading modes, namely, the clamping at the left end of the beam and symmetrical loads at both right ends of top and bottom facesheets. 1D CUF and 3D FE were used, as shown in Table 4.

The equilibrium curves are shown in Fig. 8 with numerical values in Table 5. The 3D deformed configurations are in Fig. 9.

The numerical results suggest that

- As in the previous case, the pre-peak curves match perfectly.

- Some differences are still visible in the post-peak curves. Such a result is consistent
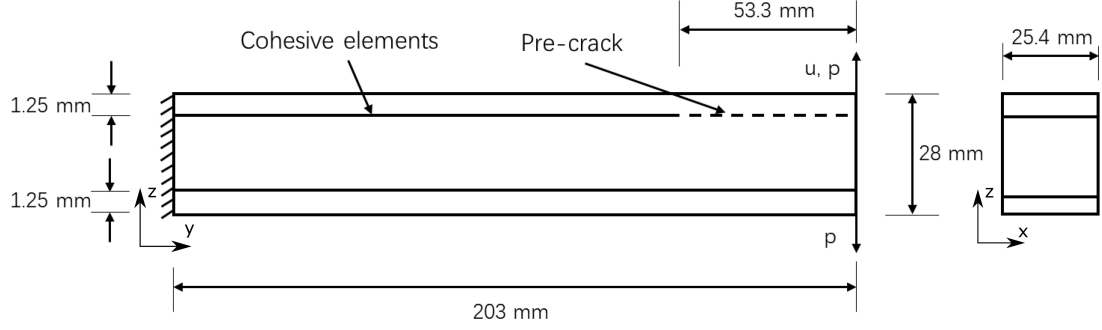
15

Figure 7: Schematic representation of the double cantilever beam (DCB) test

Table 4: Models used for the DCB

Methods	Discratisations	DOF	Time* (hh:mm:ss)
CUF	12L9-2CS6-80B4	49,980	01:33:14
ABAQUS	C3D20-COH3D8	159,096	06:57:16

* The reported run-times are based on analyses performed on a laptop using a single core.

Table 5: Load-displacement values for the DCB

Displacements [mm]	CUF [N]	ABAQUS [N]	Difference [%]
Peak load	44.776	43.870	2.07
15	42.378	42.051	0.78
20	43.577	41.896	4.01
25	38.472	37.009	3.95

16
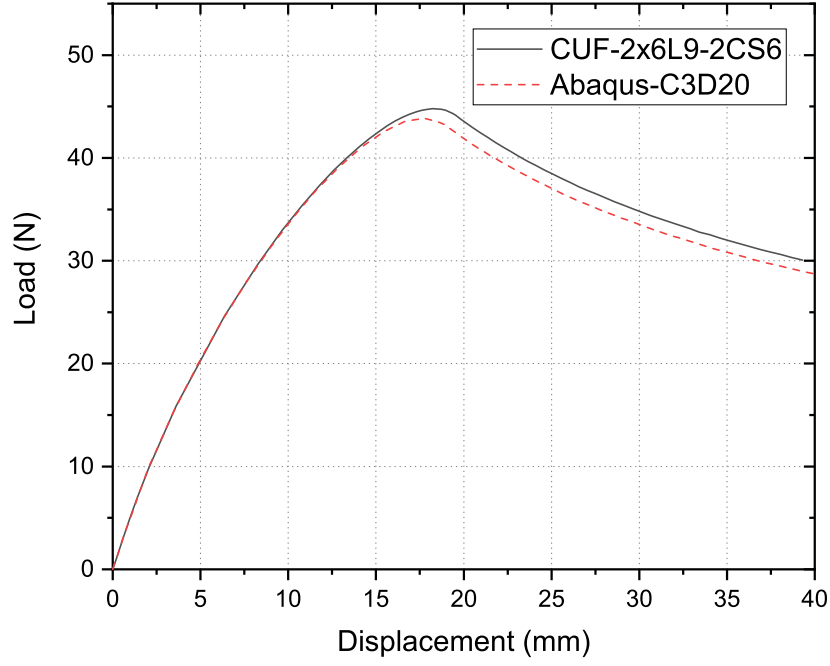
Figure 8: Load-displacement curves for the DCB test obtained by the ABAQUS and CUF approaches

(a) CUF, u=20 mm

(b) CUF, u=30 mm

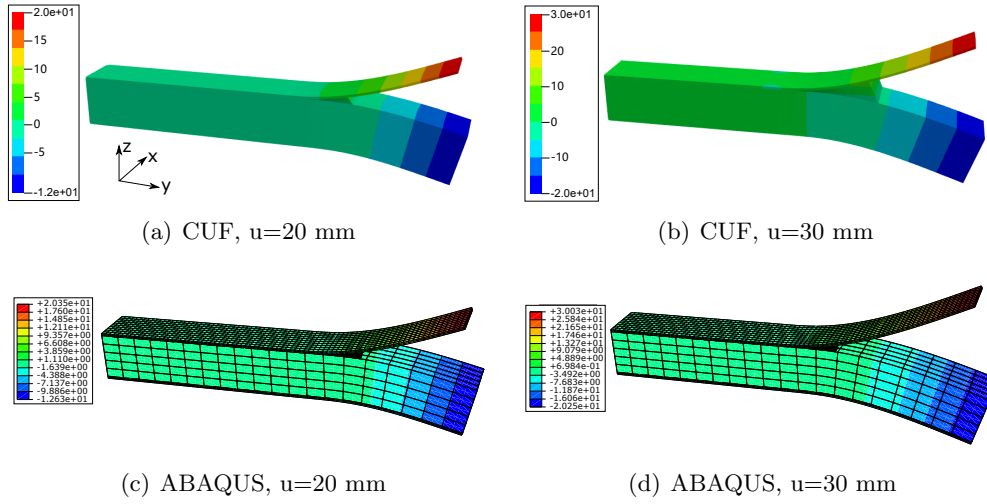(c) ABAQUS, u=20 mm

(d) ABAQUS, u=30 mm

Figure 9: 3D displacement profile of the DCB at various load levels

with the findings in [23] in which a comprehensive analysis on the effect of 1D and 3D mesh refinement was carried out to show how further 3D refinements tend to converge to the 1D solution. The 1D solution can enrich the kinematics over the cross-section without aspect ratio constraints. Therefore, very refined transverse stress fields are obtainable without the DOF overhead of 3D.

- The computational costs of 1D CUF are some 20% of 3D.

4.3 Mixed-mode bending test

The last numerical case concerns the mixed-mode bending (MMB) test. This section aims to verify the accuracy of the present formulation also for MMB. For the sake of the numerical assessment, the fracture characterization was retrieved from unidirectional composites as the authors struggled to find published literature with a complete dataset to investigate the sandwich MMB model through cohesive element theory.

The geometry of this model is shown in Fig. 10. The ratios of cohesive tractions and the energy release rates in different directions adopted in the present work are hypothetical and listed in Table 6; the other material parameters are as in the previous sections. The ratio of energy release rate is $G_{\mathrm{II}}/G_{\mathrm{T}} = 0.5$. Based on the rigid body motion assumption for the loading arm, the load-point displacement is computed as [15]

$$u = \frac{2c + L}{L} u_m - \frac{2c}{L} u_e \tag{32}$$

The cross-section mesh is 2×6L9 and 2CS6, and, along the longitudinal direction, 65 cubic elements (B4). Contact elements were added along the initial crack surface to avoid the inter-penetration. In ABAQUS, quadratic brick elements (C3D20) were employed with linear cohesive elements, see Table 7. Results are shown in Fig. 11 and Table 8 and suggest that

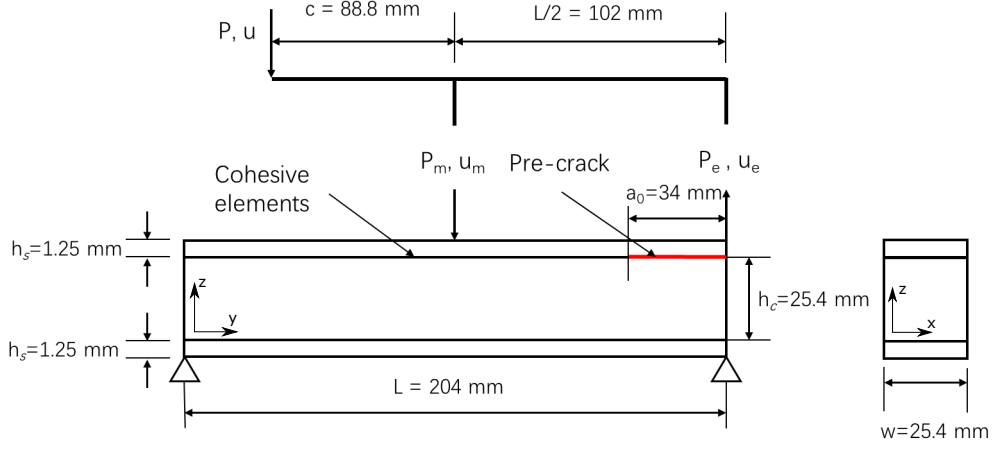- There is a good match between the two models with some differences in the post-

18

Figure 10: A schematic representation of the mixed-mode bending test (MMB)

Table 6: Parameters of the sandwich MMB [23]

Cohesive T_3 [MPa]	T_2 [MPa]	G_{Ic} [J/m^2]	G_{IIc} [J/m^2]	K_0 [MPa]
0.5	0.625	1,050	1,863	75

Table 7: Model information for the MMB

Method	Discretisation	Total element	DOF	Time* (hh:mm:ss)
CUF	12L9-2CS6-65B4	910	41,160	01:14:35
ABAQUS	C3D20R-COH3D8	20,797	171,888	09:10:20

* The reported run-times are based on analyses performed on a laptop using a single core.

19

peak regime. Such differences are similar to the previous cases.

- The computational cost of the CUF model is some 10% of the 3D FE.

Table 8: Load-displacement values for MMB

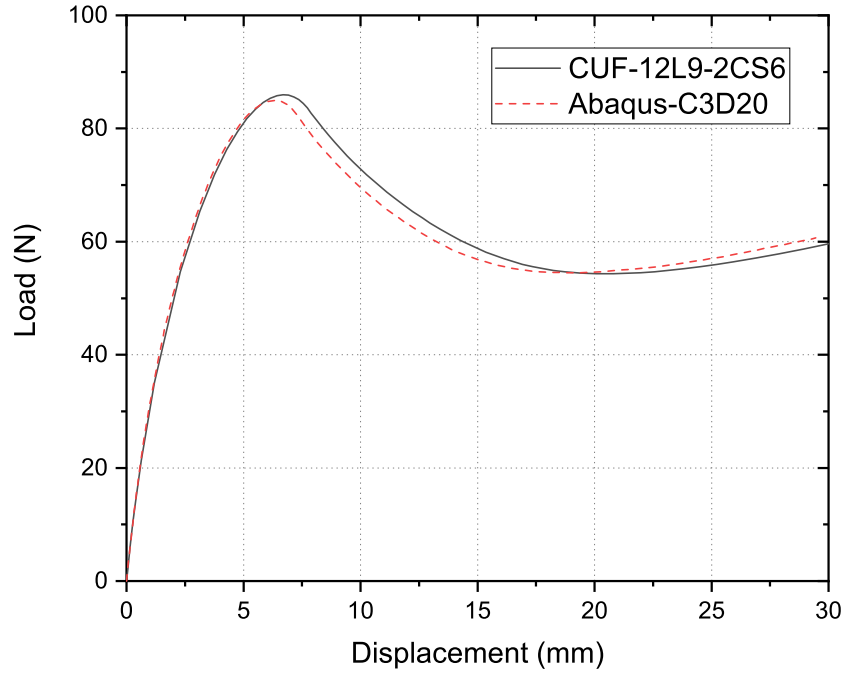| Displace [mm]	Load P [N]		Difference [%]
	CUF	ABAQUS	
Peak load	85.962	84.965	1.16
Valley load	54.302	54.483	0.33
5	80.928	81.494	0.70
10	72.835	69.581	4.47
15	58.772	56.848	3.27
20	54.358	54.612	0.47
25	55.857	57.046	2.13

Figure 11: Load-displacement curves for MMB as obtained from the ABAQUS and CUF approaches

5 Conclusions

This paper has presented numerical results concerning disbonding problems in sandwich structures. The aim has been to verify the accuracy and computational efficiency of 1D refined models; whereas, for verification and validation purposes, 3D FE and experimental data were employed. The structural formulation stems from the CUF and is based on 1D FE with Lagrange polynomials to define the cross-section kinematics. Although the presented structural modelling approach is based on a 1D formulation, the complete 3D stress field can be obtained; furthermore, the primary variables are pure displacement degrees of freedom. Disbonding of the sandwich structure is modelled using well established cohesive constitutive laws from the literature and based on works of Camanho et al. [25]. The findings of this paper highlight the accuracy and efficiency of the proposed approach, and the capability of overcoming a priori assumptions typical of 1D models. In fact,

- There is a good match between the various models with maximum differences of 3-4%. The presented numerical assessments serve as validation cases to demonstrate the capability of the proposed approach in the numerical modelling of disbonding in sandwich structures.

- The computational time of the present framework falls between 10-20% of 3D FE, thus demonstrating its computational efficiency.

- The 1D approach can provide an accurate 3D distribution of deformation and stress and does not require any a priori kinematic assumptions.

Due to the good computational efficiency, future extensions could deal with more complex structures and the introduction of multifield effects.

Declaration of Competing Interest

The authors declare that they have no known competing financial interests or personal relationships that could have appeared to influence the work reported in this paper.

Acknowledgements

References

[1] A Shipsha, M Burman, and D Zenkert. Interfacial fatigue crack growth in foam core sandwich structures. *Fatigue and fracture of engineering materials and structures (Print)*, 22(2):123–131, 1999.

[2] DL Grau, XS Qiu, and BV Sankar. Relation between interfacial fracture toughness and mode-mixity in honeycomb core sandwich composites. *Journal of Sandwich Structures and Materials*, 8(3):187–203, 2006.

[3] A Quispitupa, C Berggreen, and LA Carlsson. Fatigue debond growth in sandwich structures loaded in mixed mode bending (mmb). *ECCM13*, 2008.

[4] M Burman and D Zenkert. Fatigue of undamaged and damaged honeycomb sandwich beams. *Journal of Sandwich Structures and Materials*, 2(1):50–74, 2000.

[5] A Quispitupa, C Berggreen, and LA Carlsson. On the analysis of a mixed mode bending sandwich specimen for debond fracture characterization. *Engineering Fracture Mechanics*, 76(4):594–613, 2009.

[6] C Berggreen, BC Simonsen, and KK Borum. Experimental and numerical study of interface crack propagation in foam-cored sandwich beams. *Journal of composite materials*, 41(4):493–520, 2007.

[7] A Farshidi, C Berggreen, and R Schäuble. Numerical fracture analysis and model validation for disbonded honeycomb core sandwich composites. *Composite Structures*, 210:231–238, 2019.

[8] DS Dugdale. Yielding of steel sheets containing slits. *Journal of the Mechanics and Physics of Solids*, 8(2):100–104, 1960.

[9] GI Barenblatt. The mathematical theory of equilibrium cracks in brittle fracture. *Advances in applied mechanics*, 7(1):55–129, 1962.

[10] JP Clech, LM Keer, and JL Lewis. A crack model of a bone cement interface. *Journal of Biomechanical Engineering*, 106(3):235–243, 1984.

[11] KR Jagtap, HH Nawale, and S Roy. Delamination study of sandwich beam coupled with piezoelectric actuator using cohesive surface behavior. In *Techno-Societal 2016, International Conference on Advanced Technologies for Societal Applications*, pages 283–291, Cham, 2018. Springer.

[12] S Kozinov, M Kuna, and S Roth. A cohesive zone model for the electromechanical damage of piezoelectric/ferroelectric materials. *Smart Materials and Structures*, 23(5):055024, 2014.

[13] O Allix and P Ladevèze. Interlaminar interface modelling for the prediction of delamination. *Composite structures*, 22(4):235–242, 1992.

[14] Y Mi, MA Crisfield, G Davies, and HB Hellweg. Progressive delamination using interface elements. *Journal of composite materials*, 32(14):1246–1272, 1998.

[15] PP Camanho, CG Davila, and MF De Moura. Numerical simulation of mixed-mode progressive delamination in composite materials. *Journal of composite materials*, 37(16):1415–1438, 2003.

[16] D Höwer, BA Lerch, BA Bednarcyk, EJ Pineda, S Reese, and JW Simon. Cohesive zone modeling for mode i facesheet to core delamination of sandwich panels accounting for fiber bridging. *Composite Structures*, 183:568–581, 2018.

[17] D Höwer, KC Jois, BA Lerch, BA Bednarcyk, EJ Pineda, S Reese, and JW Simon. Relevance of 3d simulations and sandwich core topology for the modeling of honeycomb core sandwich panels undergoing interfacial crack propagation. *Composite Structures*, 202:660–674, 2018.

[18] Jing-Fen Chen, Evgeny V. Morozov, and Krishnakumar Shankar. Simulating progressive failure of composite laminates including in-ply and delamination damage effects. *Composites Part A: Applied Science and Manufacturing*, 61:185 – 200, 2014.

[19] Saman Hosseini, Joris J.C. Remmers, Clemens V. Verhoosel, and René de Borst. Propagation of delamination in composite materials with isogeometric continuum shell elements. *International Journal for Numerical Methods in Engineering*, 102(3-4):159–179, 2015.

[20] Erasmo Carrera and Angelo Ciuffreda. Bending of composites and sandwich plates subjected to localized lateral loadings: a comparison of various theories. *Composite Structures*, 68(2):185 – 202, 2005.

[21] E Carrera, M Cinefra, M Petrolo, and E Zappino. *Finite element analysis of structures through unified formulation.* John Wiley and Sons, 2014.

24

[22] E Carrera and M Petrolo. Refined beam elements with only displacement variables and plate/shell capabilities. *Meccanica*, 47(3):537–556, 2012.

[23] I Kaleel, E Carrera, and M Petrolo. Progressive delamination of laminated composites via 1d models. *Composite Structures*, 235:111799, 2020.

[24] E Carrera and M Petrolo. Refined one-dimensional formulations for laminated structure analysis. *AIAA Journal*, 50(1):176–189, 2012.

[25] A Turon, PP Camanho, J Costa, and CG Dávila. A damage model for the simulation of delamination in advanced composites under variable-mode loading. *Mechanics of materials*, 38(11):1072–1089, 2006.

[26] ML Benzeggagh and MJCS Kenane. Measurement of mixed-mode delamination fracture toughness of unidirectional glass/epoxy composites with mixed-mode bending apparatus. *Composites science and technology*, 56(4):439–449, 1996.

[27] MA Gutiérrez. Energy release control for numerical simulations of failure in quasi-brittle solids. *Communications in Numerical Methods in Engineering*, 20(1):19–29, 2004.

[28] CV Verhoosel, JJC Remmers, and MA Gutiérrez. A dissipation-based arc-length method for robust simulation of brittle and ductile failure. *International Journal for Numerical Methods in Engineering*, 77(9):1290–1321, 2009.